Available online at www.sciencedirect.com

ScienceDirect

journal homepage: www.elsevier.com/locate/he

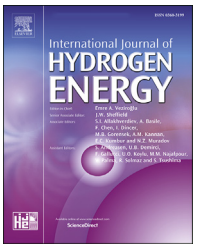

A microstructure informed and mixed-mode cohesive zone approach to simulating hydrogen embrittlement

Meichao Lin [a], Haiyang Yu [b,**], Xu Wang [a,c], Ruijun Wang [d], Yu Ding [a], Antonio Alvaro [e,f], Vigdis Olden [e], Jianying He [a], Zhiliang Zhang [a,*]

[a] Department of Structural Engineering, Norwegian University of Science and Technology (NTNU), Trondheim, 7491, Norway

[b] Division of Applied Mechanics, Department of Materials Science and Engineering, Uppsala University, Uppsala, SE-75121, Sweden

[c] College of Safety and Ocean Engineering, China University of Petroleum, Beijing, 102249, China

[d] Corrosion and Protection Center, Institute for Advanced Materials and Technology, University of Science and Technology Beijing, Beijing, 100083, China

[e] SINTEF Industry, Trondheim, 7456, Norway

[f] Department of Mechanical and Industrial Engineering, Norwegian University of Science and Technology (NTNU), Trondheim, 7491, Norway

HIGHLIGHTS

- A real microstructure-based simulation approach for hydrogen embrittlement is developed.
- The influence of hydrogen on shear strength is analyzed with mixed-mode cohesive zone model.
- The method provides a powerful tool for the interpretation of experiments on dual phase steels.
- This method can serve as a predictive material design tool towards improved hydrogen resistance.

ARTICLE INFO

Article history:
Received 2 July 2021
Received in revised form
13 January 2022
Accepted 22 March 2022
Available online 12 April 2022

Keywords:
Hydrogen embrittlement
Cohesive zone model
Duplex stainless steel
Microstructure

ABSTRACT

Hydrogen induced failure under uniaxial tension is simulated in a duplex stainless steel considering microstructural feature of the material. There are three key ingredients in the modelling approach: image processing and finite element representation of the experimentally observed microstructure, stress driven hydrogen diffusion and diffusion coupled cohesive zone modelling of fracture considering mixed failure mode. The microstructure used as basis for the modelling work is obtained from specimens cut in the transverse and longitudinal directions. It is found that the microstructure significantly influences hydrogen diffusion and fracture. The austenite phase is polygonal and randomly distributed in the transverse direction, where a larger effective hydrogen diffusion coefficient and a lower hydrogen fracture resistance is found, compared to the specimen in the longitudinal direction, where the austenite phase is slender and laminated. This indicates that the proper design and control of the austenite phase help improve hydrogen resistance of duplex stainless steel. The strength of the interface in the shear direction is found to dominate the fracture mode and initiation site, which reveals the importance of

* Corresponding author.
** Corresponding author.
E-mail addresses: haiyang.yu@angstrom.uu.se (H. Yu), zhiliang.zhang@ntnu.no (Z. Zhang).

https://doi.org/10.1016/j.ijhydene.2022.03.226

considering mixed failure mode and calibrating the hydrogen induced strength reduction in shear.

Nomenclature

σ_{cn}	Critical normal stress
σ_{ct}	Critical shear stress
δ_{cn}	Critical normal separation
δ_{ct}	Critical shear separation
D	Damage indicator
D_{max}	The largest value of D
ζ	Viscosity
$\sigma_{c,0}$	The critical cohesive stress without hydrogen
θ	Hydrogen coverage
$\sigma_{c,\theta}$	The critical cohesive stress with hydrogen
$\varphi(\theta)$	Simplified term for $\sigma_{cn,\theta}/\sigma_{cn,0}$
C	Hydrogen concentration
Δg_b^0	Gibbs free energy-difference between the surface and the bulk
R	Gas constant
C_L	Lattice hydrogen concentration
V_H	Partial molar volume
T^Z	Absoute zero temperature
σ_h	Local hydrostatic stress
C_T	Trapped hydrogen concentration
ε_p	Equivalent plastic strain
D_{eff}	Effective hydrogen diffusion coefficient
C_s	Surface hydrogen concentration
C_i	Initial bulk concentration
V_γ	Austenite volume fraction
k	The ratio to distinguish fracture type
I_{EF}	Hydrogen embrittlement index
E_F	Failure strain without hydrogen
$E_{F,\ H}$	Failure strain with hydrogen
HE	Hydrogen embrittlement
HEDE	Hydrogen enhanced decohesion
HELP	Hydrogen enhanced localized plasticity
HESIV	Hydrogen-enhanced strain-induced vacancy formation
DSS	Duplex stainless steel
LD	Longitudinal direction
TD	Transverse direction
CZM	Cohesive zone model

Introduction

Hydrogen embrittlement (HE) usually occurs abruptly and catastrophically [1,2], posing a great challenge to a number of industrial sectors, e.g., offshore, aerospace and energy industries. Continuum scale simulation is an effective tool to predict and assess HE in practical applications. Generally, three elements are essential to building a sound HE assessment tool at the continuum level, namely a sound mechanical basis, an appropriate model and a parameter calibration approach [3].

Numerous HE mechanisms have been proposed and reviewed in the literature [4–11], but a consensus is still lacking. Among these, two theories are prevailing, the hydrogen enhanced decohesion (HEDE) mechanism and the hydrogen enhanced localized plasticity (HELP) mechanism. According to the HEDE mechanism, hydrogen weakens the cohesive strength of atomic bonds in the material lattice [12] typically leading to premature separation (brittle fracture) of interfaces that are preferred traps for H, e.g. phase and precipitation interfaces and grain boundaries. The HELP mechanism, on the other hand, states that hydrogen facilitates dislocation mobility which locally enhances plasticity [13]. This enhanced plasticity can further lead to the formation of vacancies or local stress concentration, causing material separation. Some theories are proposed to address this process, such as the hydrogen-enhanced strain-induced vacancy formation mechanism (HESIV) [14] and the HELP mediated decohesion mechanism [15].

Duplex stainless steel (DSS) offers both outstanding mechanical properties and good corrosion resistance, attributed to the balanced microstructure of the austenite (γ) and the ferrite (α) phases [16–18]. Usually, rolled DSS displays distinct mechanical properties in different directions, it has higher impact energy and better ductility in the longitudinal direction (LD) than in the transverse direction (TD) [19]. The stress partitioning and plastic deformation between the two phases is dependent on the loading direction as well. By using in situ X-ray diffraction, Moverare et al. [20] found that more plastic deformation occurred in austenite during loading in TD. DSS is prone to hydrogen induced cracking despite of its excellent properties [21–23]. In the presence of hydrogen cracking tends to initiate at phase boundaries or in ferrite, with subsequent propagation along phase boundaries [21,24]. Furthermore, the microstructural features, i.e. the austenite phase size and shape are shown to influence the hydrogen diffusion coefficient and hydrogen absorption [25,26]. In rolled samples, the austenite phase shows slender shape in LD, while it has a polygonal pattern in TD [21]. The referred experimental findings qualitatively indicate that rolled DSS may have different HE sensitivity when loaded in the TD vs LD. In order to explore this quantitatively, numerical study is carried out here. The HEDE mechanism represented by a hydrogen influenced cohesive zone model is adopted for the modelling of hydrogen induced fracture at the ferrite-austenite phase boundaries.

The development of continuum scale HE assessment tool based on HEDE has been in progress for many years. HEDE is consistent with a Griffith type of fracture as in *inter-* or *trans-*granular cleavage fracture. For this study cohesive zone modelling (CZM) is a good candidate, since it can represent the brittle cleavage fracture observed in many experiments [27–33]. In the adopted model the fracture energy decreases with the increase of hydrogen content, and thus captures the premature failure in the presence of hydrogen. With the purpose of better accounting for real time hydrogen redistribution during the fracture process, a coupled diffusion and CZM approach is established [31,34,35]. It contains hydrogen transport driven by local stress and plastic strain, along with mechanical damage caused by locally accumulated hydrogen. The coupled diffusion and CZM is a reliable method for predicting hydrogen-induced fracture, which has been applied to steel [32,36], nickel [29] and additively manufactured material [27]. A more sophisticated version of this approach in 3D was reported by Alvaro et al. [37,38]. Moriconi et al. [39] and Busto et al. [40] further applied the coupled diffusion and CZM approach in cyclic loading scenario. Brocks et al. [41] proposed an approach which in addition to coupling hydrogen diffusion and CZM, accounts for hydrogen induced softening of the yield strength and the surface kinetics during hydrogen absorption. So far, merely the mode I (normal mode dominated) failure of cohesive elements has been considered in these approaches, while the influence of hydrogen on shear strength has been largely neglected [27–32]. Mixed-mode CZM has mostly been applied to composites [42–44]. The application of mixed-mode CZM to HE is still lacking.

As presented above, the CZM based HE simulation has taken into account various factors such as hydrogen redistribution, surface kinetics and different loading conditions. However, a premise of the simulation is that the material is homogenous. The heterogeneity in material microstructures, to a large extent, has been overlooked. As well understood, the complexity of HE phenomena is largely due to the complicated material microstructure [45–47]. Microstructure has been found to influence almost all the aspects of HE, such as hydrogen absorption, diffusion, trapping and crack nucleation and propagation [26,48–50]. A more sophisticated HE assessment tool therefore should take the microstructural features into consideration. This work aims to build a microstructure informed, coupled diffusion and mix-mode CZM approach to simulating HE. To begin with, a DSS as reviewed earlier is selected as the target. The two distinguishable phases, austenite (γ) and ferrite (α), possess different mechanical and hydrogen diffusion related properties [24,51]. The size and distribution patterns of the two phases induce divergent microstructural configurations, which influences the HE resistance of the material. In this work, two typical microstructures obtained from a cold rolled DSS in the LD and TD were used as the examples for the microstructural representation in the numerical model. Hydrogen induced failure behaviors of these two structures were simulated and compared.

The modelling framework is highlighted by the reconstruction of experimentally observed microstructure and the sequential combination of hydrogen diffusion and fracture. This puts the simulation and analysis under a realistic context. Furthermore, the consideration of mix-mode fracture makes it possible to probe the influence of hydrogen on shear strength, which is an important but often neglected aspect of HE.

Method

Hydrogen diffusion informed cohesive zone approach

Material failure is described by the CZM approach considering mixed (normal and shear) mode fracture. The constitutive behavior of the cohesive element is described by the so-called traction separation law (TSL). The polynomial type of TSL [52] is employed.

$$\sigma(\delta)=\begin{cases}\dfrac{27}{4}\sigma_c\dfrac{\delta}{\delta_c}\left(1-\dfrac{\delta}{\delta_c}\right)^2 & \delta\le\delta_c\\ 0 & \delta>\delta_c\end{cases} \tag{1}$$

where σ_c is the critical cohesive strength; δ_c is the critical separation; $\sigma(\delta)$ and δ are stress and separation of the cohesive element.

In order to consider mixed mode fracture, a damage indicator D, which considers the contribution from both failure modes is introduced [53].

$$D=\sqrt{\left(\frac{\delta_n}{\delta_{cn}}\right)^2+\left(\frac{\delta_t}{\delta_{ct}}\right)^2} \tag{2}$$

where δ_n and δ_t are the normal and shear separation of the cohesive elements; δ_{cn} and δ_{ct} are the critical separation in the normal and shear modes, respectively. The cohesive element fails when D reaches one. The same form of equation applies to both the normal and shear failure modes.

$$\sigma_n=\frac{27}{4}\sigma_{cn}\frac{\delta_n}{\delta_{cn}}(1-D_{max})^2 \tag{3}$$

$$\sigma_t=\frac{27}{4}\sigma_{ct}\frac{\delta_t}{\delta_{ct}}(1-D_{max})^2 \tag{4}$$

where σ_{cn} and σ_{ct} are the critical normal and shear stress, respectively. D_{max} is the largest value of damage indicator that the cohesive element has experienced. This TSL can be visualized in a 3D space as a failure surface, as shown in Fig. 1(a).

The CZM simulation is realized with a user defined element (UEL) subroutine, developed by Scheider et al. [53] and revised by the current authors. It is worth mentioning that a convergence problem is often encountered in CZM simulation, due to numerical instability, making it impractical to track the post-instability behavior of the simulated structure [54]. This problem is particularly evident in microstructure informed model where the geometry is rather complicated. A feasible solution to this issue is to introduce a viscosity-like component into the constitutive equation of the cohesive element to regularize the numerical instability [54].

$$\sigma(\delta)=\frac{27}{4}\sigma_c\frac{\delta}{\delta_c}\left(1-\frac{\delta}{\delta_c}\right)^2+\zeta\frac{d}{dt}\left(\frac{\delta}{\delta_c}\right) \tag{5}$$

where ζ is viscosity. This approach is shown to have negligible influence on the global behavior of the structure given that ζ is

sufficiently small [55]. In this work, it is determined based on a convergence study and applies to both the normal and shear direction.

The hydrogen effect is reflected in the CZM approach by decreasing the critical cohesive strength with increasing hydrogen content [28,30,36], while keeping the critical separation constant. A hydrogen influenced cohesive law applicable in DSS [30,32,56] is used in current work.

$$\frac{\sigma_{cn,\,\theta}}{\sigma_{cn,\,0}} = 1 - 1.0467\theta + 0.1687\theta^2 \tag{6}$$

$$\theta = \frac{C}{C + exp\left(-\Delta g_b^0/RT\right)} \tag{7}$$

where $\sigma_{cn,\,0}$ is the critical cohesive stress without hydrogen; θ is the hydrogen coverage; $\sigma_{cn,\,\theta}$ is the critical cohesive stress with hydrogen; C is the hydrogen concentration; Δg_b^0 is the Gibbs free energy-difference between the surface and the bulk; R is the gas constant; T is the temperature. Hereinafter, $\sigma_{cn,\,\theta}/\sigma_{cn,\,0}$ is defined as $\varphi(\theta)$ for simplification. This equation is proposed originally for normal fracture mode, in this work it is also extended to shear mode. The corresponding hydrogen degraded TSL with different hydrogen coverage θ is illustrated in Fig. 1 (b). The influence of hydrogen on shearing failure has not been explicitly considered by CZM. In CZM simulation of large-scale experiments considering a combined failure mode, the influence of hydrogen in the shear direction is usually omitted [30]. This is mainly because the observed shear features in the presence of hydrogen, e.g., shear lips, are usually attributed to micro-void process and so show a ductile nature [57]. At the microscale, hydrogen promoted shearing failure in metallic material is also related to dislocation activity. Hydrogen promotes the pileup of dislocations at the interface like grain and phase boundaries and can induce shear fracture, as illustrated in Ref. [30], which is consistent with the HELP mechanism. In such cases where an actual interface exists, applying a hydrogen modified shear failure mode in CZM is sensible, and can be regarded as a simple phenomenological representation of the HELP mediated decohesion mechanism in the shear direction. Due to the lack of data in literature, two scenarios were designed for demonstration, a scenario where the hydrogen degraded shear strength followed the same function as the normal strength, $\sigma_{ct,\theta} = \varphi(\theta) \times \sigma_{ct,0}$, and a scenario where the hydrogen degraded strength in shear direction was only 80% of that in normal direction, $\sigma_{ct,\,\theta} = 0.8 \times \varphi(\theta) \times \sigma_{ct,0}$. As will be elaborated later, shear fracture is enhanced in the latter scenario, which led to a notable change in the fracture behavior compared to the former.

To consider the redistribution of hydrogen, stress driven hydrogen diffusion is simulated, following the control equation [36]:

$$\frac{\partial C_L}{\partial t} = D_d \nabla^2 C_L + \frac{D_d V_H}{R\left(T - T^Z\right)} \nabla C_L \nabla \sigma_h + \frac{D_d V_H}{R\left(T - T^Z\right)} C_L \nabla^2 \sigma_h \tag{8}$$

where C_L is the lattice hydrogen concentration; V_H is the partial molar volume; R is the gas constant; T^Z is the absolute zero temperature; T is the temperature; σ_h is the local hydrostatic stress acquired by finite element analysis. Trapped hydrogen concentration due to plastic strain is represented as a simplified function of the lattice concentration, following Olden et al. [25,30].

$$C_T = \left(49.0\varepsilon_p + 0.1\right) \cdot C_L \tag{9}$$

where C_T is the trapped hydrogen concentration; ε_p is the equivalent plastic strain.

The real time hydrogen concentration obtained via the stress driven hydrogen diffusion analysis is then used as a reference for determining the cohesive strength, following Eq. (6). The coupled diffusion and CZM approach is realized in three steps [29,36]:

(I) Elastic-plastic finite element simulation. The model is loaded without hydrogen to the target deformation level, yielding detailed information of the stress field throughout the loading history.
(II) Stress-driven mass diffusion analysis. The pre-charged hydrogen redistributes according to stress field obtained in (I), providing real time hydrogen contour.
(III) CZM simulation taking into account the hydrogen distribution as obtained through Eqs. (8) and (9) and the hydrogen degradation to the normal and shear failure modes.

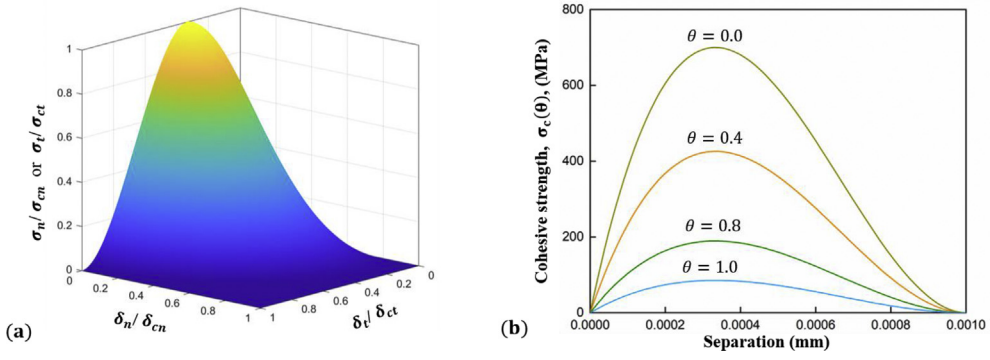

Fig. 1 – (a) The 3-D profile of TSL considering mixed mode failure; (b) Hydrogen degraded TSL for normal fracture mode with different hydrogen coverage θ.

Modelling of microstructural feature

The finite element models were based on a square section (200 μm × 200 μm) optically observed from a typical 2205 DSS specimen. Four models, the LD, LD-90, TD and TD-90, were considered, as presented in Fig. 2(a–d). Note that LD-90 and TD-90 represent rotation of LD and TD by 90°, respectively. In these optical microscopy images, the austenite (γ) phase appears bright, while the ferrite (α) phase appears dark, consistent with the magnetic force microscopy (MFM) results reported in Refs. [16,17,58]. The mechanical properties of these two phases, were shown in Fig. 3(a) [59,60]. Hydrogen diffusion properties were listed in Table 1. The diffusivity of hydrogen in the austenite phase is five orders of magnitude lower than that in ferrite, while the solubility is three orders of magnitude higher.

The models were built strictly following the patterns displayed in Fig. 2. This was achieved by converting the optical microscopy images into duotone figures and then using a script to generate finite element mesh and insert cohesive elements along the phase interfaces. The corresponding duotone figures were presented in Fig. 2(a1-d1). The models were meshed with about 30,000 elements. The zoom-in views of selected finite element mesh were illustrated in Fig. 2(b2-c2).

Numerical procedure

The simulation is implemented in ABAQUS with a UEL subroutine. Hydrogen diffusion without stress was first simulated using the square models illustrated in Fig. 2, representing the hydrogen pre-charging procedure. 1 wppm of hydrogen was initially supplied on the top surface.

To consider stress driven hydrogen diffusion, two rectangular regions of 200 μm × 40 μm were further cut from the LD-90 and TD square models, as indicated by the red frames in Fig. 2(b and c). The two sections were selected in the way that they had almost an equal volume fraction of austenite (40.7% for LD-90 vs 38.4% for TD). A simulated pre-charged stage (stress free hydrogen diffusion) was applied for 100 h, with 1 wppm of hydrogen applied on the left and right surfaces, as illustrated in Fig. 3(b). The pre-charged models were then subjected to tensile loading with insulated boundary conditions, resulting in hydrogen redistribution inside the models through Eqs. (8) and (9). For mass diffusion analysis, DC2D3 and DC2D4 elements were used in Abaqus; for stress analysis, the matrix is meshed with CPS3 and CPS4 elements.

Table 1 – Parameters for the hydrogen diffusion analysis [21,25,61].

Diffusivity (m^2s^{-1})	Solubility ($ppm\ mm\ N^{-1/2}$)	Δg_b^0 (kJ/mol)	R (J/mol/K)	T (K)
Austenite, γ: 1.4×10^{-16}	Austenite, γ: 32.51	30	8.314	298
Ferrite, α: 6.0×10^{-11}	Ferrite, α: 0.033			

At last, fracture in the selected rectangular sections in the presence of hydrogen was simulated using the hydrogen informed CZM approach. Different ratios of $\sigma_{ct,0}/\sigma_{cn,0}$ was considered to investigate the influence of normal and shear strength on fracture initiation. Two scenarios of hydrogen degradation on cohesive strength were considered, as detailed in subsection 2.1. In scenario 1, hydrogen decreased the shear and normal strength equally; in scenario 2, the reduction in shear strength was more severe than the normal strength. Intuitively, shear failure is more important in scenario 2, which helps demonstrate the significance of considering hydrogen degradation in shear.

Results and discussion

Effect of microstructure on hydrogen diffusion

The profiles of hydrogen distribution in different models after pre-charging are shown in Fig. 4. Hydrogen was supplied on the top surface, and a variety of pre-charging times were examined. Comparing subfigures (a) and (b) to subfigures (c) and (d), the global hydrogen diffusion in the transversely models (TD and TD-90) is much faster than in the longitudinally models (LD and LD-90). Specifically, the TD and TD-90 models have been fully charged with hydrogen after approximately 400 h, while the time required for the LD-90 and LD models are more than 2000 h.

It is known that the hydrogen diffusion coefficient is higher, and the solubility is lower in ferrite [21,25], indicating that austenite acts as a diffusion barrier and largely influences the global hydrogen transport. This can be quantified by an effective diffusion coefficient D_{eff}, taking into account the volume fraction, size and alignment of austenite phase in the whole model. Thick plate assumption is adopted in the calculation of D_{eff} [62]. According to the following equation, hydrogen content is a function of time and distance from the charging surface.

$$C(x,t) = C_i + (C_s - C_i)\left[1 - erf\left(\frac{x}{2\sqrt{D_{eff}t}}\right)\right] \tag{10}$$

$$erf(u) = \frac{2}{\sqrt{\pi}}\int_0^u \exp(-u^2)du \ \text{ and } \ u = \frac{x}{2\sqrt{D_{eff}t}} \tag{11}$$

where x is the distance from the charging surface; C_s is the surface hydrogen concentration; C_i is the initial bulk concentration; t is the charging time. The time variation of the normalized hydrogen concentration on the bottom surface is plotted in Fig. 5. When the value reaches half the hydrogen concentration on the top surface, Eq. (10) is simplified to Eq. (12).

$$x = \sqrt{D_{eff}t} \tag{12}$$

D_{eff} can therefore indicate the "global speed" of hydrogen distribution. The calculated D_{eff} for different models are listed in Table 2. The values are in reasonable agreement with the results reported in other work [21,25,62], where the diffusion

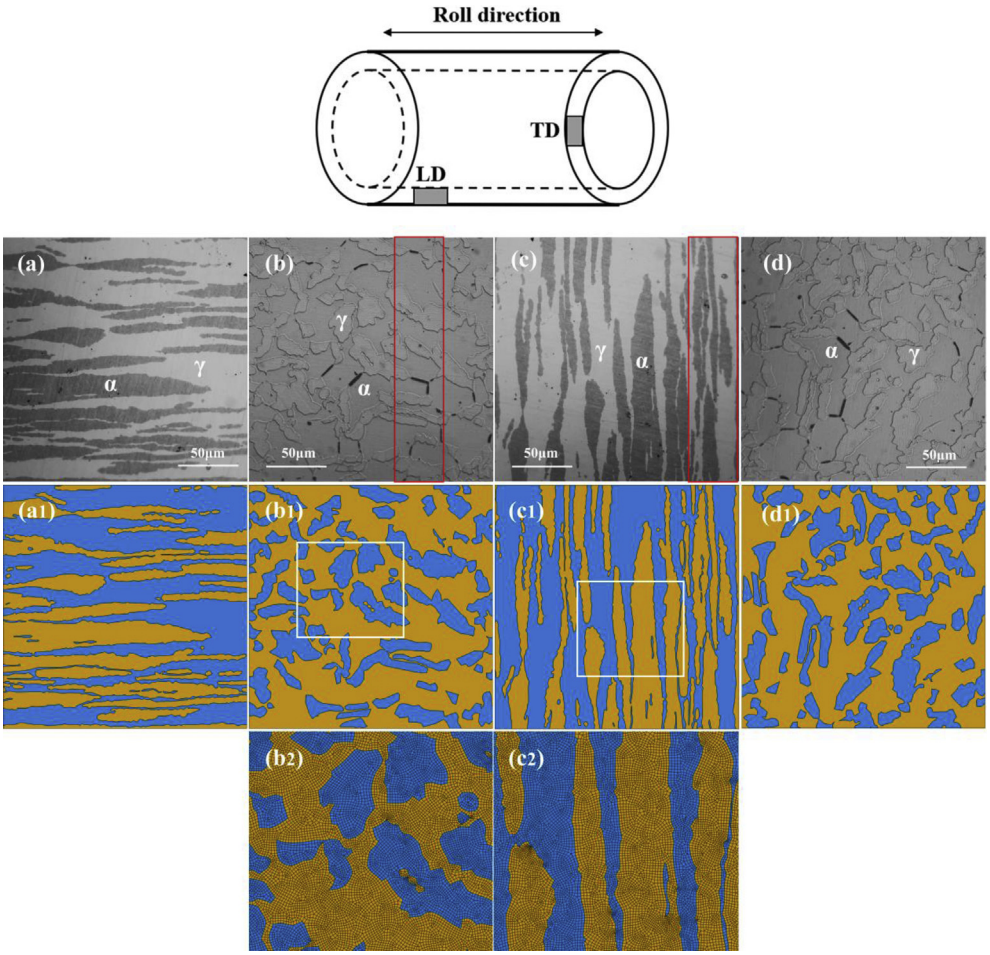

Fig. 2 – (a)–(d) Microstructures in different directions: LD, TD, LD-90 and TD-90, respectively; (a1)-(d1) The corresponding microstructure based finite element models; (b2)-(c2) Enlarged views of finite element mesh marked with white square frame in (b1) and (c1); The red frames in (b), (c) show selected rectangular regions for stress driven diffusion and CZM simulation. (For interpretation of the references to colour in this figure legend, the reader is referred to the Web version of this article.)

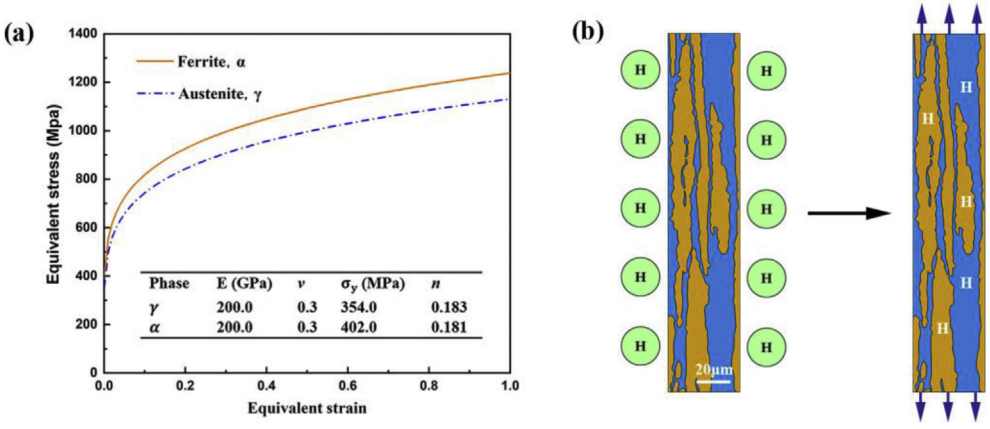

Fig. 3 – (a) Mechanical properties for ferrite and austenite reproduced from the data in Refs. [59,60]; (b) Illustration of pre-charging and stress driven diffusion process. Note that the models here are cut from Fig. 2(b) and (c).

coefficients are in the range of 10^{-16}–10^{-12} m^2/s. D_{eff} in the TD model is two orders of magnitude higher than that in the LD model and one order higher than in the LD-90 model. Again, hydrogen diffuses faster in transversely directed structures than in longitudinally directed ones. As also listed in Table 2, the austenite volume fraction (V_γ) in the TD and LD models are

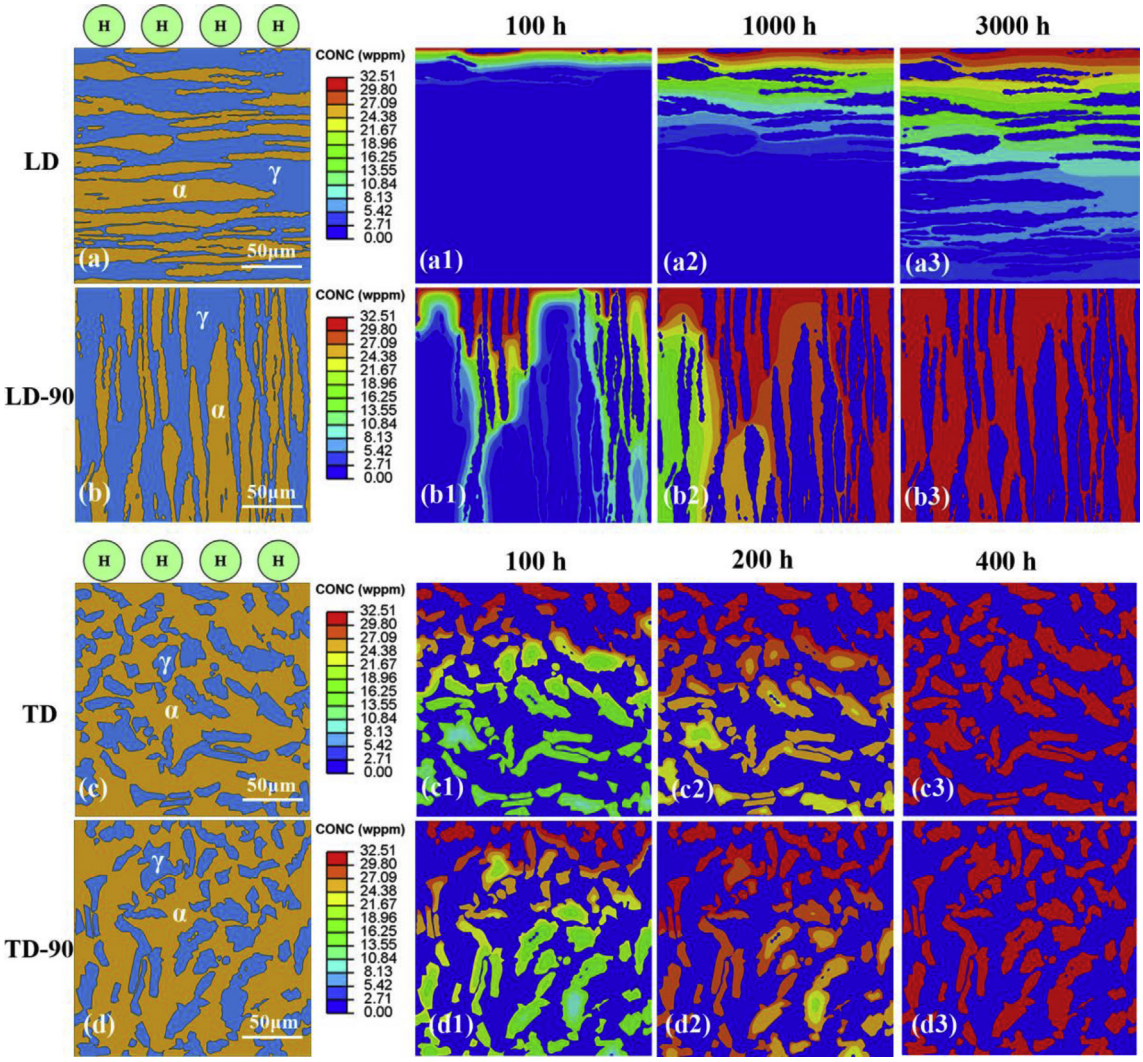

Fig. 4 – Hydrogen distribution contours after pre-charging for different times: (a)-(a3) LD; (b)-(b3) LD-90; (c)-(c3) TD; (d)-(d3) TD-90.

approximately equal, 38.4% and 40.7%, respectively. Therefore, the difference in D_{eff} is not attributable to the difference in V_{γ}. It is rather the microstructural features, i.e. the size and distribution of the austenite phase, that is responsible for the different global hydrogen transportation properties. Similar conclusion is drawn in Refs. [21,25,62].

Comparing Fig. 4(a) and (b) to Fig. 4(c) and (d), we see a clear difference in the distribution of the austenite phase in the transversely and longitudinally models. In the longitudinally models, the austenite phase has slender shape and appears in a laminated pattern, the layers of austenite are continuous and spread across the entire model. This effectively isolates the ferrite phase in which hydrogen diffuses orders of magnitude faster. In other words, the fast hydrogen diffusion paths are cut in the longitudinally models. In the LD model, the paths are blocked to the largest extent, therefore we observe the smallest D_{eff}, an order of magnitude smaller than that in the LD-90 model. In contrast, the austenite phase has polygonal shape and distributes in a random manner in the transversely models, which leaves sufficient fast diffusion channels, i.e. the ferrite phase, that are continuous from the top surface to the bottom. Due to the randomness of the distribution, the TD and TD-90 models have the same magnitude of effective diffusion coefficient. All these microstructural observations match the quantitative analysis of the effective diffusion coefficient.

The analysis in this part reveals the importance of microstructures on the absorption of hydrogen, which is an important topic in HE study [26]. More specifically, in DSS, the austenite phase could be engineered in order to increase the accelerated ferrite inherent diffusion path, leading to advantages with respect to hydrogen permeation.

Effect of microstructure on stress driven hydrogen diffusion

Hydrogen induced degradation of material properties are in practice often manifested as premature fracture under loading in tension. In this modelling procedure, hydrogen redistributes according to the material stress and strain field, concentrates at certain locations and weakens the structure

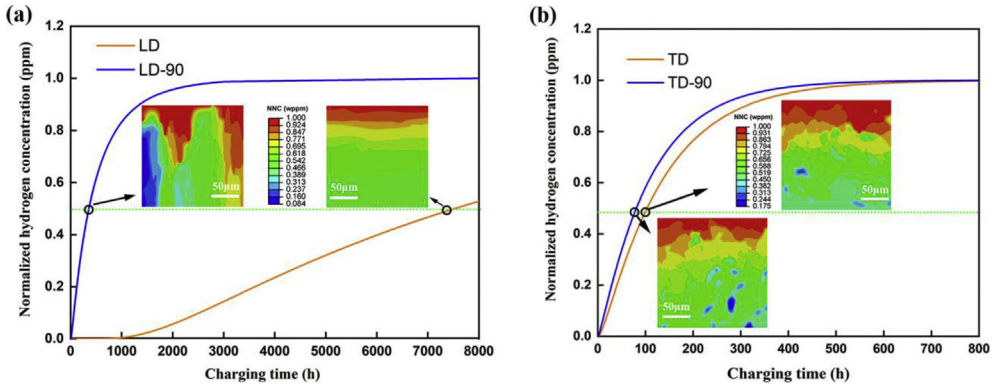

Fig. 5 – Variation of the normalized hydrogen concentration on the bottom surface with charging time: (a) LD and LD-90; (b) TD and TD-90. The insets show the normalized hydrogen concentration contour at the marked charging time.

Table 2 – D_{eff} and V_γ in different models.

Model	LD	LD-90	TD	TD-90
D_{eff} (m^2/s)	3.70×10^{-16}	7.80×10^{-15}	2.68×10^{-14}	3.43×10^{-14}
V_γ (%)	40.7%	40.7%	38.4%	38.4%

Note: LD-90 and TD-90 have same V_γ as LD and TD.

locally. The process is heavily dependent on the microstructural features. It is therefore important to study the hydrogen redistribution under loading, taking the microstructural characteristics into account. For this purpose, the rectangular shape of LD-90 and TD models were adopted, as elaborated in Section: Method. The models were first 'pre-charged' with hydrogen (stress free hydrogen diffusion) for 100 h, with hydrogen initially supplied on the longitudinal side surfaces; subsequently tensile loading was applied in the longitudinal direction; insulated boundary conditions were applied during the loading process, so that there was no hydrogen outgassing. The strategy is illustrated in Fig. 3(b).

The distribution of von Mises stress and equivalent plastic strain (PEEQ) at the end of loading with 10% applied strain are shown in Fig. 6(a and b) and Fig. 7(a and b), respectively. The stress is concentrated in the ferrite phase for both models, which makes sense as ferrite has higher yield strength and flow stress than austenite (Fig. 3(a)). This is also consistent with experimental results using in-situ digital imaging correlation (DIC) technique [49] that shows the ferrite phase carries higher load than the austenite phase in hydrogen-free samples. The PEEQ distribution provides evidence that austenite holds more plasticity than ferrite, matching the in-situ neutron diffraction result [51] illustrating that austenite experiences higher dislocation density during tensile test. The maximum von Mises stress in the TD model is 915.7 MPa and 852.8 MPa in the LD-90 model. The difference is not deemed significant considering the randomness of the phase distribution in the microstructure.

The hydrogen distribution after pre-charging for 100 h in the LD-90 and TD models is shown in Figs. 6(c) and Fig.7(c), respectively. For the sake of clarity the hydrogen distribution in ferrite and austenite phases is presented in two separate figures, isolating the ferrite and austenite from each other (see Fig. 6(d1,d3) and Fig. 7(d1,d3)). Since the effective hydrogen diffusion coefficient is much larger in the TD than that in the LD-90 model (Table 2), the total hydrogen amount in the TD is larger than in the LD-90 model after pre-charging.

Hydrogen distribution at the end of loading with 10% applied strain are shown in Fig. 6(d2, d4) for LD-90 and Fig. 7(d2, d4) for TD model, respectively. The overall hydrogen concentration increases in ferrite and decreases in austenite upon loading. In Refs. [21,59], the diffusible hydrogen is also observed to become more concentrated in ferrite upon loading. The average hydrogen concentration in ferrite increases from 0.028 to 0.034 wppm for LD-90, while from 0.03 to 0.036 wppm for TD. This indicates that hydrogen flows from austenite to ferrite with applied stress, thus accumulating in the ferrite phase and at phase boundaries. It is well established that hydrogen-induced crack initiates at stress-concentrating and hydrogen accumulating sites [24,59]. Recalling that the stress is also concentrated in the ferrite phase, it is then expected that hydrogen induced cracking initiates close to or in the ferrite phase, which is consistent with the experimental observations [21,32,49,63].

Fracture in the absence of hydrogen

Cohesive elements are inserted along phase boundaries, as indicated by the red lines in Fig. 8(b) and Fig. 9(b). Normal and shear degradation accumulates simultaneously in the fracture process zone during loading. Complete failure occurs when Eq. (2) reaches one. The critical normal stress, $\sigma_{cn,0}$, is set as the experimental tensile strength reported in the literature

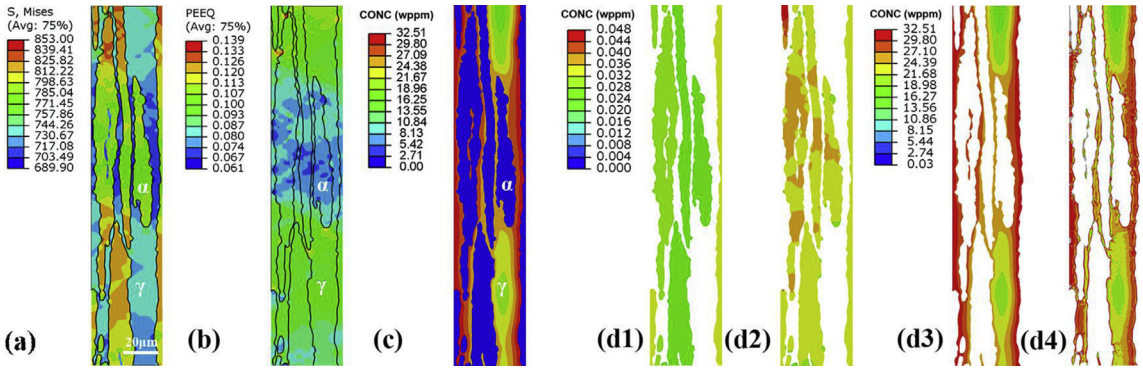

Fig. 6 – LD-90 model: (a) von Mises stress, and (b) PEEQ distribution at applied strain 10%; (c) Hydrogen distribution after pre-charging for 100 h and before straining; (d1, d3) Separated views of hydrogen distribution in ferrite and austenite before straining; (d2, d4) Separated views of hydrogen distribution in ferrite and austenite after straining.

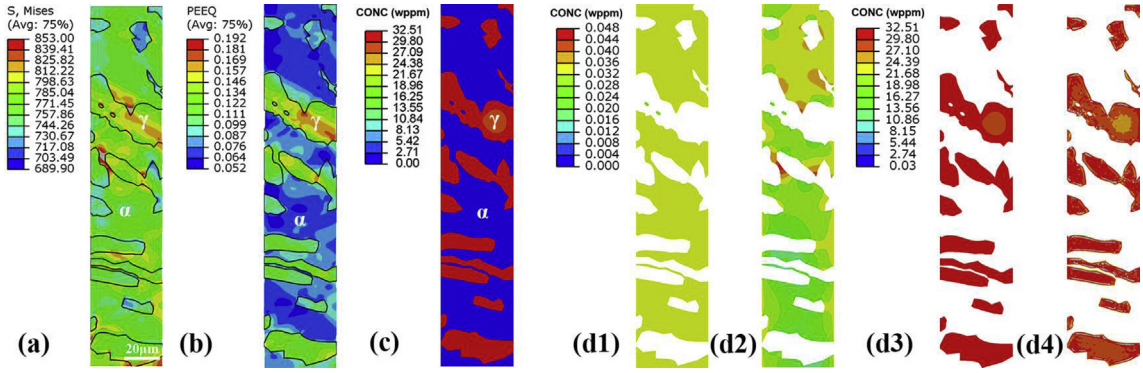

Fig. 7 – TD model: (a) von Mises stress, and (b) PEEQ distribution at applied strain 10%; (c) Hydrogen distribution after pre-charging for 100 h and before straining; (d1, d3) Separated views of hydrogen distribution in ferrite and austenite before straining; (d2, d4) Separated views of hydrogen distribution in ferrite and austenite after straining.

[59,60]. According to Ref. [64], the shear strength is about 50–80% of the tensile strength for steel. The critical shear stress, $\sigma_{ct,0}$, is hence set as 50–80% of $\sigma_{cn,0}$. We also consider two extreme cases where $\sigma_{ct,0}$ is much smaller, just 20% and 30% of $\sigma_{cn,0}$, for comparison. The parameters used for CZM are listed in Table 3.

The nominal stress-strain curves of the LD-90 and TD models simulated with CZM are presented in Fig. 8(a) and Fig.9(a). As expected, failure occurs earlier with decreasing $\sigma_{ct,0}$ in both models. In addition, TD yields lower tensile strength, as well as lower failure strain than LD-90. For TD the cohesive zone elements are mainly vertical to the loading direction, while for LD-90 they are mainly parallel to the loading direction. Consequently, it is easier for TD to reach the failure criterion in Eq. (2). This demonstrates how the orientation of the microstructure may influence the mechanical properties of DSS.

The failure site is taken as the position where the damage indicator (D) first reaches 1. In LD-90, two different crack sites are found, as shown in Fig. 8(c–d). As for TD, four different crack sites are identified, as shown in Fig. 9(c–f). This implicates that the weakest site changes with different $\sigma_{ct,0}$. Obviously, the weakest site also depends on the microstructure. Moreover, with the decrease in $\sigma_{ct,0}$, a change in the fracture mode, from normal dominated to shear dominated, is captured. To quantitatively distinguish the type of fracture, a criterion based on δ_t/δ_{ct} and δ_n/δ_{cn} is employed.

Chao et al. [65,66] established a fracture criterion for cracks under mixed-mode load, the failure type is determined by comparing τ_{max}/σ_{max} at a fixed distance around crack tip to material stress ratio τ_C/σ_C, with $\tau_{max}/\sigma_{max} < \tau_C/\sigma_C$ indicating a normal type of fracture and $\tau_{max}/\sigma_{max} > \tau_C/\sigma_C$ indicating a shear type of fracture. Inspired by this, the fracture type in this work is determined by comparing δ_t/δ_{ct} at the crack site to δ_n/δ_{cn}, with $\delta_t/\delta_{ct} < \delta_n/\delta_{cn}$ indicating normal dominated fracture, and $\delta_t/\delta_{ct} > \delta_n/\delta_{cn}$ indicating shear dominated fracture. This idea is illustrated in Fig. 10. For convenience, a ratio $k = (\delta_t/\delta_{ct})/(\delta_n/\delta_{cn})$ is introduced to distinguish the fracture type, with $k<1$ being normal dominated fracture and $k>1$ being shear dominated fracture.

The value of k in different conditions are listed in Table 4. In the absence of hydrogen, k increases with decreasing $\sigma_{ct,0}$ in both models, meaning that the shear fracture becomes increasingly important with a declining $\sigma_{ct,0}$. The normal dominated fracture changes to shear dominated fracture when $\sigma_{ct,0}$ decreases to 20% of $\sigma_{cn,0}$ in the LD-90, showing the ratio of $\sigma_{ct,0}/\sigma_{cn,0}$ determines the failure type. However, the change of fracture mode happens when $\sigma_{ct,0}$ is 30% of $\sigma_{cn,0}$ for

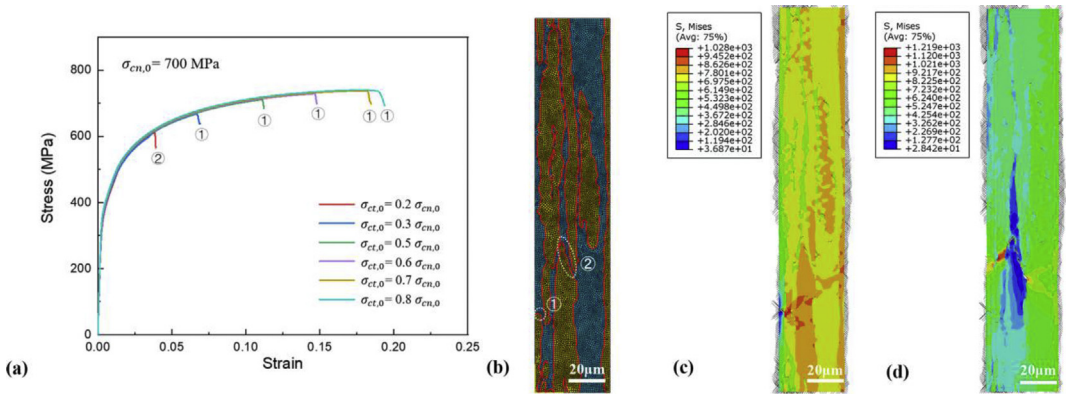

Fig. 8 – LD-90 model: (a) Nominal stress-strain curves; (b) Illustration of cohesive zone elements and crack sites; (c) Crack site ① at $\sigma_{ct,0} = 0.5\ \sigma_{cn,0}$; (d) Crack site ② at $\sigma_{ct,0} = 0.2\ \sigma_{cn,0}$; The black flakes in (c) (d) represent the user defined cohesive elements.

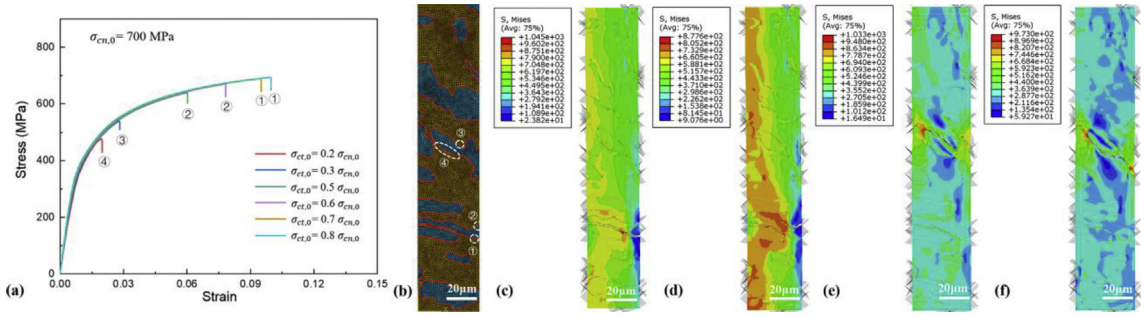

Fig. 9 – TD model: (a) Nominal stress-strain curves; (b) Illustration of cohesive zone elements and crack sites; (c) Crack site ① at $\sigma_{ct,0} = 0.8\ \sigma_{cn,0}$; (d) Crack site ② at $\sigma_{ct,0} = 0.6\ \sigma_{cn,0}$; (e) Crack site ③ at $\sigma_{ct,0} = 0.3\ \sigma_{cn,0}$; (f) Crack site ④ at $\sigma_{ct,0}$ 0.2 $\sigma_{cn,0}$; The black flakes in (c)–(f) represent the user defined cohesive elements.

Table 3 – Parameters used for CZM simulation.

No Hydrogen		
$\sigma_{cn,0}$: 700 MPa	δ_{cn}: 0.001 mm	δ_{ct}: 0.001 mm
$\sigma_{ct,0}$: 0.8 $\sigma_{cn,0}$, 0.7 $\sigma_{cn,0}$, 0.6 $\sigma_{cn,0}$, 0.5 $\sigma_{cn,0}$, 0.3 $\sigma_{cn,0}$, 0.2 $\sigma_{cn,0}$		
With Hydrogen		
Scenario 1: $\sigma_{cn,\theta} = \varphi(\theta) \times \sigma_{cn,0}$,	$\sigma_{ct,\theta} = \varphi(\theta) \times \sigma_{ct,0}$	
Scenario 2: $\sigma_{cn,\theta} = \varphi(\theta) \times \sigma_{cn,0}$,	$\sigma_{ct,\theta} = 0.8 \times \varphi(\theta) \times \sigma_{ct,0}$	

TD. Fig. 8(a and b) and Fig. 9(a and b) show that the failure site changes along with the switch of failure type. Regarding the normal dominated fracture, failure initiates at the cohesive interface vertical to the loading direction, e.g., crack site ① for LD-90, crack site ① and ② for TD; as for shear dominated fracture, the interface is approximately 45° to the loading direction, e.g., crack site ② for LD-90, crack site ③ and ④ for TD. These observations are reasonable considering that the normal component of loading reaches the maximum in the former case while the shear component reaches the maximum in the latter.

Fracture in the presence of hydrogen

Fracture in the presence of hydrogen was simulated with the three-step approach elaborated earlier. The total hydrogen concentration, $C_T + C_L$, at the CZM interface was determined using transient hydrogen diffusion analysis. The normal strength of the CZM interface was then decreased with hydrogen concentration according to Eq. (6). Two scenarios were designed to consider hydrogen degraded shear strength, as illustrated in Table 3. More details about the modelling procedure are found in Section: Method.

As expected, failure occurs earlier in the presence of hydrogen, in both scenarios and both the LD-90 and TD models, but the failure mode and fracture site can differ. In scenario 1, the change in failure mode occurs at the same ratio of $\sigma_{ct,0}/\sigma_{cn,0}$, as the case with no hydrogen, as shown in Table 4. This is because the ratio of $\sigma_{ct,\theta}/\sigma_{cn,\theta}$ in scenario 1 stays constant in the presence of hydrogen and equal to the case with no hydrogen. As described in the previous section, the failure mode is governed by this ratio. Due to the same reason, we observe no difference in the fracture sites either.

In scenario 2, we observe a difference in the ratio of $\sigma_{ct,0}/\sigma_{cn,0}$ at which the failure mode changes. For LD-90, normal dominated fracture changes to shear dominated fracture when $\sigma_{ct,0}$ is 30% of $\sigma_{cn,0}$, see Table 4; in TD, the transition occurs when $\sigma_{ct,0}$ is 50% of $\sigma_{cn,0}$. In the absence of hydrogen, the values are 20% and 30%, respectively. It is consistent with the imposed conditions of $\sigma_{ct,\theta}/\ \sigma_{cn,\theta} = 0.8 \times \sigma_{ct,0}/\ \sigma_{cn,0}$ in this scenario. As an example for LD-90, 30% $\sigma_{cn,0} \times 0.8 = 24\%\ \sigma_{cn,0}$ in scenario 2 is close to the ratio of 20% in the absence of

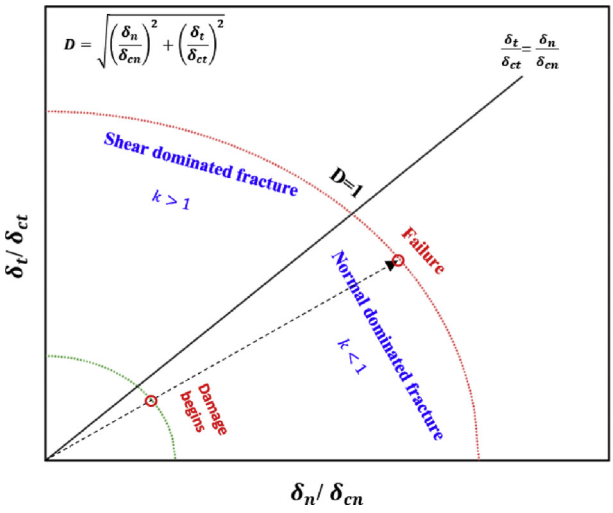

Fig. 10 – Illustration of failure type, with $k < 1$ being normal dominated fracture and $k > 1$ being shear dominated fracture.

hydrogen. Again, this shows that the failure mode of the model is dominated by the ratio between the normal and shear strength at failure.

In LD-90, the failure site is different compared to the hydrogen free case with $\sigma_{ct,0}/\sigma_{cn,0} = 0.3$, as presented in Fig. 11, where failure initiates at site ② which has shear dominated fracture instead of site ① that has normal dominated fracture. In TD, similarly, a change in the failure site is also observed, but in the $\sigma_{ct,0}/\sigma_{cn,0} = 0.5$ case, as illustrated in Fig. 12. Here, failure initiates at site ③, which has shear dominated fracture instead of site ② that has normal dominated fracture. Again, this is consistent with the failure mode transition discussed earlier. These simulation results shows that there is a direct link between the fracture site and the failure mode. If a different fracture site is observed in the presence of hydrogen, it usually indicates hydrogen also influences the failure mode. To verify this in practice, the in-situ micro tensile testing [67] can be a good approach.

In order to quantitatively compare the HE susceptibility of LD-90 and TD, an index based on failure strain is adopted to evaluate the influence of microstructure on HE sensitivity [68].

$$I_{EF} = \left(1 - \frac{E_{F,H}}{E_F}\right) \times 100\% \quad (13)$$

where I_{EF} is the HE index; E_F is the nominal failure strain without hydrogen; $E_{F,H}$ is the nominal failure strain with hydrogen. The value of I_{EF} for the two microstructures in scenario 1 and scenario 2 are listed in Table 5. It is found that I_{EF} in scenario 2 is always larger than that in scenario 1. In addition, TD yields larger I_{EF} than LD-90 in both scenarios. The average I_{EF} are 0.3549 for TD vs 0.1424 for LD-90 in scenario 1, and 0.4212 vs 0.2476 in scenario 2. It indicates that TD is more susceptible to HE under the current loading direction. As discussed previously, TD accumulates more hydrogen and therefore undergoes more severe degradation of the mechanical property. This is a clear indication of the importance of microstructure in the HE sensitivity of DSS.

Further, we note that some experiments suggested that a finer austenite spacing is favorable for improved HE resistance of material [49]. Concerning the microstructure of the two models presented in this paper, the austenite phase takes a slender shape in LD-90 and has smaller spacing compared with that in the TD, i.e. microstructure with smaller austenite spacing is less sensitive to HE. This agrees qualitatively with the experimental finding [49]. Meanwhile, it should also be noted that the current simulation results are still insufficient to draw a definitive conclusion on realistic material. To verify the assumption, more simulations with different microstructures and loading conditions should be conducted, and an in-situ tensile experiment capable of tracking the fracture initiation site is also needed.

Summary

Hydrogen informed finite element CZM simulation considering the influence of microstructure is performed. Two microstructure configurations of DSS are modelled based on optical micrographs. Mixed failure modes are considered in the CZM analysis, which capture the complexity in failure along the irregular phase interfaces between ferrite and austenite. The methodology developed in this work can easily be applied to other microstructures, as well as other scenarios, such as hydrogen induced intergranular failure in a polycrystal, and the interfacial separation at a precipitate. In this paper the proposed modelling methodology is used toward the investigation of hydrogen diffusion and fracture properties in a dual phased models in a parametric study manner and the main conclusions are as follows.

(1) The effective hydrogen diffusion coefficient is highly dependent on the microstructural features. The effective diffusion coefficient in the model with polygonal shaped austenite phases is one to two orders of

Table 4 – The value of k in different conditions.

	LD-90			TD		
	NO H	Scenario 1	Scenario 2	NO H	Scenario 1	Scenario 2
$\sigma_{ct,0} = 0.8\ \sigma_{cn,0}$	0.4659	0.3840	0.3977	0.1444	0.2926	0.3117
$\sigma_{ct,0} = 0.7\ \sigma_{cn,0}$	0.5891	0.3982	0.3984	0.2228	0.3100	0.3426
$\sigma_{ct,0} = 0.6\ \sigma_{cn,0}$	0.9431	0.9234	0.9571	0.3436	0.3168	0.3360
$\sigma_{ct,0} = 0.5\ \sigma_{cn,0}$	0.9823	0.9656	0.9703	0.3600	0.3530	1.3580
$\sigma_{ct,0} = 0.3\ \sigma_{cn,0}$	0.9858	0.9663	2.8515	1.5055	1.5031	1.8118
$\sigma_{ct,0} = 0.2\ \sigma_{cn,0}$	3.1689	2.9951	3.0403	1.5170	1.2815	1.8097

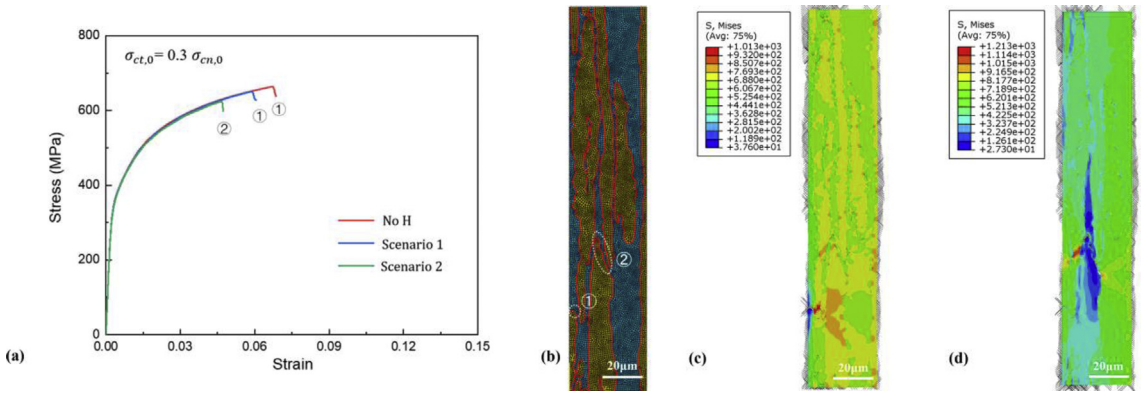

Fig. 11 – LD-90 model: (a) Nominal stress-strain curves; (b) Illustration of cohesive zone elements and crack sites; (c) Crack site ① in scenario 1; (d) Crack site ② in scenario 2.

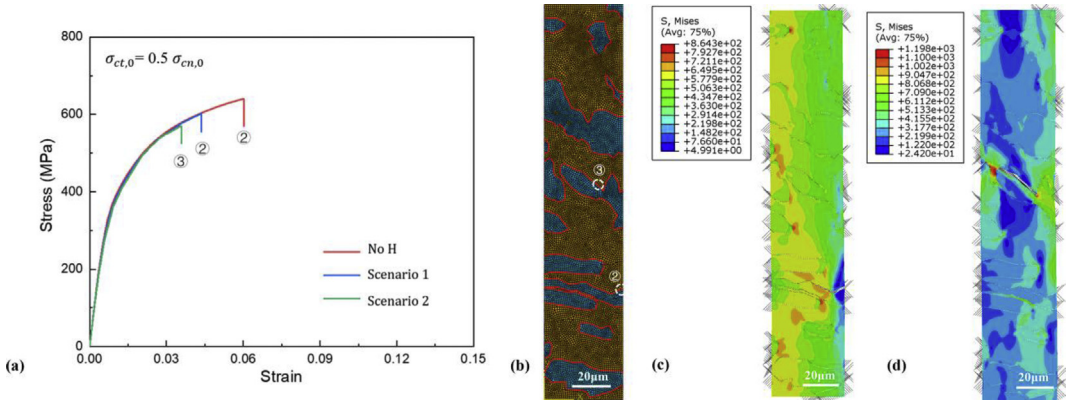

Fig. 12 – TD model: (a) Nominal stress-strain curves; (b) Illustration of cohesive zone elements and crack site; (c) Crack site ② in scenario 1; (d) Crack site ③ in scenario 2.

Table 5 – I_{EF} for LD-90 and TD models in scenario 1 and scenario 2.

	LD-90		TD	
	Scenario 1	Scenario 2	Scenario 1	Scenario 2
$\sigma_{ct,0} = 0.8\ \sigma_{cn,0}$	0.0544	0.2609	0.3256	0.4283
$\sigma_{ct,0} = 0.7\ \sigma_{cn,0}$	0.1875	0.3397	0.4243	0.4869
$\sigma_{ct,0} = 0.6\ \sigma_{cn,0}$	0.2071	0.3287	0.4047	0.4615
$\sigma_{ct,0} = 0.5\ \sigma_{cn,0}$	0.1824	0.2762	0.3477	0.4030
$\sigma_{ct,0} = 0.3\ \sigma_{cn,0}$	0.1211	0.1610	0.3038	0.3638
$\sigma_{ct,0} = 0.2\ \sigma_{cn,0}$	0.1018	0.1192	0.3235	0.3835
Average	**0.1424**	**0.2476**	**0.3549**	**0.4212**

magnitude larger than for the model with elongated austenite phases. This is attributed to the austenite phase which acts as the barrier to hydrogen diffusion. Upon loading, hydrogen tends to move from the austenite phase to the ferrite phase, driven by the higher stress built in the ferrite phase.

(2) In the CZM simulation without hydrogen, we found that the shear strength of material interface influences the fracture initiation location and failure mode. In general, fracture initiates mainly due to stress in the normal direction if the shear strength is close to the normal strength, but shear dominated fracture can appear if the shear strength is lower than 50% of the normal strength.

(3) In the presence of hydrogen, failure is promoted as a result of hydrogen reduced interfacial strength. The influence of hydrogen on the shear strength is found to have a significant influence on the location of fracture initiation and the associated fracture mode. The fracture mode is generally unaffected if hydrogen reduces the normal and shear strength following the same relation, and shear failure is promoted if hydrogen reduces the shear strength to a larger extent. This suggests that a proper calibration of the hydrogen influence on the shear strength is critical, in order to accurately model the hydrogen induced mixed failure at the microscale, which is still missing. It is further shown

that loading the model paralleling to the elongated austenite phase yields better resistance to hydrogen induced failure.

These conclusions are drawn based on the finite element simulation of the selected microstructure and loading direction. Although the microstructure has been explicitly modelled in this work, there is a certain level of simplification to the model, for instance, fracture is limited to the phase interfaces, hydrogen trapped at the interfaces due to precipitates and lattice distortions is not captured, and only one kind of boundary condition is considered. There is still a line between the simulation results and real material behavior. In the future, systematic numerical study considering various microstructures and boundary conditions will be performed.

Declaration of competing interest

The authors declare that they have no known competing financial interests or personal relationships that could have appeared to influence the work reported in this paper.

Acknowledgements

The authors appreciate the support provided by Research Council of Norway through the HyLINE (294739) and M-HEAT (294689) projects.

REFERENCES

[1] Wu X, Zhang H, Yang M, Jia W, Qiu Y, Lan L. From the perspective of new technology of blending hydrogen into natural gas pipelines transmission: mechanism, experimental study, and suggestions for further work of hydrogen embrittlement in high-strength pipeline steels. Int J Hydrogen Energy 2022;47:8071–90.
[2] Ustolin F, Paltrinieri N, Berto F. Loss of integrity of hydrogen technologies: a critical review. Int J Hydrogen Energy 2020;45:23809–40.
[3] Yu H, Olsen JS, Alvaro A, Qiao L, He J, Zhang Z. Hydrogen informed Gurson model for hydrogen embrittlement simulation. Eng Fract Mech 2019;217:106542.
[4] Barrera O, Bombac D, Chen Y, Daff TD, Galindo-Nava E, Gong P, et al. Understanding and mitigating hydrogen embrittlement of steels: a review of experimental, modelling and design progress from atomistic to continuum. J Mater Sci 2018;53:6251–90.
[5] Dwivedi SK, Vishwakarma M. Hydrogen embrittlement in different materials: a review. Int J Hydrogen Energy 2018;43:21603–16.
[6] Martin ML, Dadfarnia M, Nagao A, Wang S, Sofronis P. Enumeration of the hydrogen-enhanced localized plasticity mechanism for hydrogen embrittlement in structural materials. Acta Mater 2019;165:734–50.
[7] Robertson IM, Sofronis P, Nagao A, Martin ML, Wang S, Gross DW, et al. Hydrogen embrittlement understood. Metall Mater Trans 2015;46:2323–41.
[8] Li X, Ma X, Zhang J, Akiyama E, Wang Y, Song X. Review of hydrogen embrittlement in metals: hydrogen diffusion, hydrogen characterization, hydrogen embrittlement mechanism and prevention. Acta Metall Sin 2020;33:759–73.
[9] Venezuela J, Liu Q, Zhang M, Zhou Q, Atrens A. A review of hydrogen embrittlement of martensitic advanced high-strength steels. Corrosion Rev 2016;34:153–86.
[10] Djukic MB, Bakic GM, Sijacki Zeravcic V, Sedmak A, Rajicic B. The synergistic action and interplay of hydrogen embrittlement mechanisms in steels and iron: localized plasticity and decohesion. Eng Fract Mech 2019;216:106528.
[11] Ohaeri E, Eduok U, Szpunar J. Hydrogen related degradation in pipeline steel: a review. Int J Hydrogen Energy 2018;43:14584–617.
[12] Oriani RA. Mechanistic theory of hydrogen embrittlement of steels. Ber bunsenges phys chem; (Germany, federal republic of). Medium: X; Size; 1972. p. 848–57.
[13] Birnbaum HK, Sofronis P. Hydrogen-enhanced localized plasticity—a mechanism for hydrogen-related fracture. Mate Sci Eng A 1994;176:191–202.
[14] Nagumo M. Hydrogen related failure of steels – a new aspect. Mater Sci Technol 2004;20:940–50.
[15] Nagao A, Dadfarnia M, Somerday BP, Sofronis P, Ritchie RO. Hydrogen-enhanced-plasticity mediated decohesion for hydrogen-induced intergranular and "quasi-cleavage" fracture of lath martensitic steels. J Mech Phys Solid 2018;112:403–30.
[16] Guo LQ, Lin MC, Qiao LJ, Volinsky AA. Duplex stainless steel passive film electrical properties studied by in situ current sensing atomic force microscopy. Corrosion Sci 2014;78:55–62.
[17] Lin MC, Wang G, Guo LQ, Qiao LJ, Volinsky AA. Electro-mechanical coupling of semiconductor film grown on stainless steel by oxidation. Appl Phys Lett 2013;103:143118.
[18] Sobol O, Nolze G, Saliwan-Neumann R, Eliezer D, Boellinghaus T, Unger WES. Novel approach to image hydrogen distribution and related phase transformation in duplex stainless steels at the sub-micron scale. Int J Hydrogen Energy 2017;42:25114–20.
[19] Jebaraj AV, Kumar LA, Deepak CR. Investigations on anisotropy behavior of duplex stainless steel AISI 2205 for optimum weld properties. Procedia Eng 2017;173:883–90.
[20] Moverare JJ, Odén M. Influence of elastic and plastic anisotropy on the flow behavior in a duplex stainless steel. Metall Mater Trans 2002;33:57–71.
[21] Tao P, Gong J, Wang Y, Cen W, Zhao J. Modeling of hydrogen diffusion in duplex stainless steel based on microstructure using finite element method. Int J Pres Ves Pip 2020;180:104031.
[22] Elhoud AM, Renton NC, Deans WF. Hydrogen embrittlement of super duplex stainless steel in acid solution. Int J Hydrogen Energy 2010;35:6455–64.
[23] Craidy P, Briottet L, Santos D. Hydrogen–Microstructure–Mechanical properties interactions in super duplex stainless steel components. Int J Hydrogen Energy 2015;40:17084–90.
[24] Yakubov V, Lin M, Volinsky AA, Qiao L, Guo L. The hydrogen-induced pitting corrosion mechanism in duplex stainless steel studied by current-sensing atomic force microscopy. npj Mater Degrad 2018;2.
[25] Olden V, Saai A, Jemblie L, Johnsen R. FE simulation of hydrogen diffusion in duplex stainless steel. Int J Hydrogen Energy 2014;39:1156–63.
[26] Cho L, Sulistiyo DH, Seo EJ, Jo KR, Kim SW, Oh JK, et al. Hydrogen absorption and embrittlement of ultra-high strength aluminized press hardening steel. Mate Sci Eng A 2018;734:416–26.

[27] Sung S-J, Pan J, Korinko PS, Morgan M, McWillliams A. Simulations of fracture tests of uncharged and hydrogen-charged additively manufactured 304 stainless steel specimens using cohesive zone modeling. Eng Fract Mech 2019;209:125–46.
[28] Cui TC, Shang J, Hua ZL, Peng WZ, Shi JF, Xu P, et al. A coupled cohesive modeling approach for predicting fractures in low alloy steel under high-pressure hydrogen gas. Int J Hydrogen Energy 2021;46:2702–15.
[29] Yu H, Olsen JS, Olden V, Alvaro A, He J, Zhang Z. Cohesive zone simulation of grain size and misorientation effects on hydrogen embrittlement in nickel. Eng Fail Anal 2017;81:79–93.
[30] Olden V, Thaulow C, Johnsen R, Østby E, Berstad T. Influence of hydrogen from cathodic protection on the fracture susceptibility of 25%Cr duplex stainless steel – constant load SENT testing and FE-modelling using hydrogen influenced cohesive zone elements. Eng Fract Mech 2009;76:827–44.
[31] Jemblie L, Olden V, Akselsen OM. A coupled diffusion and cohesive zone modelling approach for numerically assessing hydrogen embrittlement of steel structures. Int J Hydrogen Energy 2017;42:11980–95.
[32] Olden V, Thaulow C, Johnsen R, Østby E. Cohesive zone modeling of hydrogen-induced stress cracking in 25% Cr duplex stainless steel. Scripta Mater 2007;57:615–8.
[33] Singh DK, Maiti SK, Bhandakkar TK, Raman RKS. Cohesive zone based axisymmetric modelling of hydrogen-assisted cracking in a circumferentially notched tensile specimen. Int J Hydrogen Energy 2018;43:12530–42.
[34] Jemblie L, Olden V, Akselsen OM. A review of cohesive zone modelling as an approach for numerically assessing hydrogen embrittlement of steel structures. Phil Trans Math Phys Eng Sci 2017;375:20160411.
[35] Gobbi G, Colombo C, Miccoli S, Vergani L. A fully coupled implementation of hydrogen embrittlement in FE analysis. Adv Eng Software 2019;135:102673.
[36] Yu H, Olsen JS, Alvaro A, Olden V, He J, Zhang Z. A uniform hydrogen degradation law for high strength steels. Eng Fract Mech 2016;157:56–71.
[37] Alvaro A, Olden V, Akselsen OM. 3D cohesive modelling of hydrogen embrittlement in the heat affected zone of an X70 pipeline steel. Int J Hydrogen Energy 2013;38:7539–49.
[38] Alvaro A, Olden V, Akselsen OM. 3D cohesive modelling of hydrogen embrittlement in the heat affected zone of an X70 pipeline steel – Part II. Int J Hydrogen Energy 2014;39:3528–41.
[39] Moriconi C, Hénaff G, Halm D. Cohesive zone modeling of fatigue crack propagation assisted by gaseous hydrogen in metals. Int J Fatig 2014;68:56–66.
[40] del Busto S, Betegón C, Martínez-Pañeda E. A cohesive zone framework for environmentally assisted fatigue. Eng Fract Mech 2017;185:210–26.
[41] Brocks W, Falkenberg R, Scheider I. Coupling aspects in the simulation of hydrogen-induced stress-corrosion cracking. Procedia IUTAM 2012;3:11–24.
[42] Eltaher MA, Wagih A. Micromechanical modeling of damage in elasto-plastic nanocomposites using unit cell representative volume element and cohesive zone model. Ceram Int 2020;46:10469–80.
[43] Charles Y, Estevez R, Bréchet Y, Maire E. Modelling the competition between interface debonding and particle fracture using a plastic strain dependent cohesive zone. Eng Fract Mech 2010;77:705–18.
[44] Dimitri R, Trullo M, De Lorenzis L, Zavarise G. Coupled cohesive zone models for mixed-mode fracture: a comparative study. Eng Fract Mech 2015;148:145–79.
[45] Dadfarnia M, Nagao A, Wang S, Martin ML, Somerday BP, Sofronis P. Recent advances on hydrogen embrittlement of structural materials. Int J Fract 2015;196:223–43.
[46] Martiniano GA, Silveira Leal JE, Rosa GS, Bose Filho WW, Piza Paes MT, Franco SD. Effect of specific microstructures on hydrogen embrittlement susceptibility of a modified AISI 4130 steel. Int J Hydrogen Energy 2021;46:36539–56.
[47] Egels G, Mujica Roncery L, Fussik R, Theisen W, Weber S. Impact of chemical inhomogeneities on local material properties and hydrogen environment embrittlement in AISI 304L steels. Int J Hydrogen Energy 2018;43:5206–16.
[48] Okayasu M, Fujiwara T. Effects of microstructural characteristics on the hydrogen embrittlement characteristics of austenitic, ferritic, and γ–α duplex stainless steels. Mate Sci Eng A 2021;807:140851.
[49] Örnek C, Reccagni P, Kivisäkk U, Bettini E, Engelberg DL, Pan J. Hydrogen embrittlement of super duplex stainless steel – towards understanding the effects of microstructure and strain. Int J Hydrogen Energy 2018;43:12543–55.
[50] Díaz A, Cuesta II, Rodríguez C, Alegre JM. Influence of non-homogeneous microstructure on hydrogen diffusion and trapping simulations near a crack tip in a welded joint. Theoretical and Applied Fracture Mechanics; 2021. p. 112.
[51] Liang XZ, Zhao G-H, Dodge MF, Lee TL, Dong HB, Rivera-Díaz-Del-Castillo PEJ. Hydrogen embrittlement in super duplex stainless steels. Materialia 2020;9:100524.
[52] Needleman A. A continuum model for void nucleation by inclusion debonding. J Appl Mech 1987;54:525–31.
[53] Scheider I. Cohesive model for crack propagation analyses of structures with elastic–plastic material behavior Foundations and implementation. GKSS research center Geesthacht, Dept WMS.; 2001.
[54] Gao YF, Bower AF. A simple technique for avoiding convergence problems in finite element simulations of crack nucleation and growth on cohesive interfaces. Model Simulat Mater Sci Eng 2004;12:453–63.
[55] Yu H, Olsen JS, Olden V, Alvaro A, He J, Zhang Z. Viscous regularization for cohesive zone modeling under constant displacement: an application to hydrogen embrittlement simulation. Eng Fract Mech 2016;166:23–42.
[56] Serebrinsky S, Carter E, Ortiz M. A quantum-mechanically informed continuum model of hydrogen embrittlement. J Mech Phys Solid 2004;52:2403–30.
[57] Matsuo T, Yamabe J, Matsuoka S. Effects of hydrogen on tensile properties and fracture surface morphologies of Type 316L stainless steel. Int J Hydrogen Energy 2014;39:3542–51.
[58] Guo LQ, Lin MC, Qiao LJ, Volinsky AA. Ferrite and austenite phase identification in duplex stainless steel using SPM techniques. Appl Surf Sci 2013;287:499–501.
[59] Ogita G, Matsumoto K, Mochizuki M, Mikami Y, Ito K. Evaluation of hydrogen-induced cracking behavior in duplex stainless steel by numerical simulation of stress and diffusible hydrogen distribution at the microstructural scale. Tetsu-To-Hagane 2020;106:214–23.
[60] Ogita G, Matsumoto K, Mochizuki M, Mikami Y, Ito K. Numerical simulation on effect of microstructure on hydrogen-induced cracking behavior in duplex stainless steel weld metal. ISIJ Int 2021;61(4):1236–44.
[61] Nguyen O. Coarse-graining and renormalization of atomistic binding relations and universal macroscopic cohesive behavior. J Mech Phys Solid 2002;50:1727–41.
[62] Olden V, Thaulow C, Johnsen R. Modelling of hydrogen diffusion and hydrogen induced cracking in supermartensitic and duplex stainless steels. Mater Des 2008;29:1934–48.
[63] Chou S-L, Tsai W-T. Effect of grain size on the hydrogen-assisted cracking in duplex stainless steels. Mate Sci Eng A 1999;270:219–24.

[64] Bhardwaj B. Handbook on steel bars, wires, tubes, pipes, S.S. Sheets production with ferrous metal casting & processing. Niir Project Consultancy Services; 2014.
[65] Chao YJ, Liu S. Int J Fract 1997;87:201–23.
[66] Liu S, Chao YJ, Zhu X. Tensile-shear transition in mixed mode I/III fracture. Int J Solid Struct 2004;41:6147–72.
[67] Wang D, Lu X, Wan D, Guo X, Johnsen R. Effect of hydrogen on the embrittlement susceptibility of Fe–22Mn-0.6C TWIP steel revealed by in-situ tensile tests. Mate Sci Eng A 2021:802.
[68] Briottet L, Moro I, Lemoine P. Quantifying the hydrogen embrittlement of pipeline steels for safety considerations. Int J Hydrogen Energy 2012;37:17616–23.